


Article

Experimental and Numerical Simulation Investigation on Deep Drawing Process of Inconel 718 with and without Intermediate Annealing Thermal Treatments

Unai Ulibarri, Lander Galdos, Eneko Sáenz de Argandoña and Joseba Mendiguren * 

Department of Mechanical and Industrial Production, Mondragon Unibertsitatea, Loramendi 4, 20500 Mondragon, Spain; unai.ulibarri@gmail.com (U.U.); lgaldos@mondragon.edu (L.G.); esaenzdeargan@mondragon.edu (E.S.d.A.)

* Correspondence: jmendiguren@mondragon.edu

Received: 30 October 2019; Accepted: 8 January 2020; Published: 13 January 2020



Abstract: The aeronautical industry is moving from high-capacity large-airplane construction to low-capacity small-airplane construction. With the change in the production volume, there is a need for more efficient manufacturing processes, such as stamping/deep drawing. However, the streamlined shape and exotic materials of airplanes pose a challenge to accurate numerical simulation of the manufacturing processes. In the case of the Inconel 718 material, researchers previously proposed numerical models; however, these models failed to take account of some key parameters, such as the degradation of the elastic modulus and intermediate annealing thermal processes. The aim of the present study was to characterize the Inconel 718 material, with and without intermediate annealing thermal treatment (TT) and to propose a suitable model. To evaluate the accuracy of the proposed model, a U-drawing benchmark test was used.

Keywords: Inconel 718; Inco718; springback; bauschinger; autoform

1. Introduction

The aeronautical industry has long been one of the leading players in the development and implementation of new high-added-value, advanced materials [1]. The big margin on manufacturing cost compared to the material and performance has made difficultly shaped components and the extensive use of trial and error methodologies in the manufacturing process characteristic of this sector. Clear examples to reduce that effort are the work of Groche and Backer [2] on stretch forming and the work of Zhan et al. [3] on Ti-alloy tube bending. Global mobility trends, together with tightening of the economy, have led to a departure in aircraft manufacturing from big planes (e.g., A380 and Boeing 747) to the current trend of a large number of smaller aircraft (e.g., A320 or smaller) [4]. This change in product volume has increased the importance of manufacturing costs relative to overall costs within the sector.

Driven by such change, numerous aeronautical component producers have been exploring the use of automotive-based technologies to reduce manufacturing costs, while maintaining quality [5]. In this regard, stamping (or deep drawing) is one of the most cost-effective manufacturing processes for sheet metal components used in aircraft fuselage and engines [6]. The migration from traditional forming processes to mass production stamping base processes has given rise to various issues due to the high springback. Traditionally, aeronautical components are characterized by a very streamlined and small curvature design and are manufactured with high- or very-high-strength material. These two features increase the springback after forming exponentially [7]. To address these issues, thermal

treatments (TTs) are commonly employed in an effort to reduce residual stresses or improve formability. The sector is in need of high-volume manufacturing processes that allow for intermediate TTs.

Previous research demonstrated the importance of finite element methods in efficient design and optimization of cold stamping processes [7]. In recent years, much effort has focused on the modelling of aeronautical-grade stamping operations [8]. However, due to the innate secrecy of the sector, little published information on this topic is available. In the case of Inconel 718, some information is available on the elasto–plastic modelling of stamping operations. For example, Algarni et al. [9] studied the ductile fracture of bulk Inconel 718, and Gustafsson et al. [10] modelled the behaviour of the material at intermediate temperatures using kinematic hardening models. The most comprehensive work on modelling Inconel 718 material was published by Ragai et al. [11]. They analysed and modelled the springback behaviour of Inconel 718 used in the aerospace industry. In their hardening model, they assumed constant elastic behaviour, with a Hill48 yield function and a Bauschinger effect. Later research proved that a decrease in the apparent elastic modulus had a critical impact on springback simulations [12]. Other studies showed that this phenomenon, which appeared to be related to dislocation pile-up [13], increased springback after forming [14]. The friction conditions during draw-in of the material were shown to be equally important [7].

To our knowledge, there are no studies on the impact of intermediate annealing TTs on material behaviour. Therefore, in terms of aeronautical requirements, it is not possible to accurately predict the forming behaviour and subsequent springback of components of Inconel 718 after intermediate annealing TTs. In the present study, the behaviour of Inconel 718 material in its as-received (AR) state and post-stretching TT (PSTT) state was analysed and modelled. First, potential microstructural changes due to the annealing TT were analysed. Second, the elasto–plasticity behaviour of the material (i.e., elastic behaviour, plastic yielding, hardening and necking limit) was characterized under both AR and PSTT conditions. Third, the material behaviour was modelled and used as an input for deep drawing simulations. Finally, U-drawing benchmark experimental tests were conducted, and the accuracy of the different models developed was evaluated.

2. Materials and TTs

Inconel 718 material (HAYNES[®]718; Haynes International) (hereafter, Inco718) was used. The material (1.645 mm thick) was supplied in a solution annealed state. Its chemical composition is shown in Table 1.

Table 1. Chemical composition of the Inco718 material (wt.%).

Al	B	C	Co	Cr	Cu	Fe	Mn	Mo
0.65	0.004	0.049	0.37	18.10	0.04	18.6	0.22	3.07
Ni	P	S	Si	Ti	Ta	Bi	Pb	Ag
52.9	<0.005	<0.002	0.08	1.04	<0.05	<0.00003	<0.0005	<0.0002

The material specifications defined by the material supplier are defined in Table 2.

Table 2. Material specifications provided by the material supplier.

Elastic Modulus (GPa)	σ_y (MPa)	σ_u (MPa)	Elongation (%)	Hardness (HRB)	ASTM
200	419	871	46	92.4	6-8

According to the supplier, Inco718 has a Young's modulus of 200 GPa, with a yielding stress value of 419 MPa and ultimate stress value (real stress at σ_u) of 871 MPa. The material has a ductility (elongation) of 46% at the point of necking, a grain size of 6–8 ASTM and hardness of 92.4 HRB.

Figure 1 shows the difference in the material in its AR state and PSTT state (i.e., after deformation and annealing) in a simple tensile test.

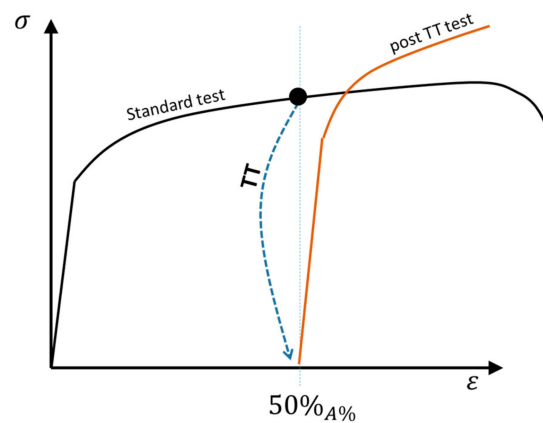


Figure 1. Difference between the as-received (AR) state and post-stretching thermal treatment (PSTT) state shown as a post-TT test.

The standard test corresponds to the AR condition, whereas the PSTT condition corresponds to the material after it had been stretched by up to 50% of its total elongation capability (50% of R_m elongation) and subsequently annealed. In the intermediate annealing process, the holding time was 6 min under 980 °C, followed by air-cooling at room temperature. As the material had an elongation to R_m of about 46% of plastic strain, a limit of 22% of plastic strain was taken as the pre-stretch for the PSTT samples.

To evaluate whether the intermediate annealing process changed the microstructure beyond the relaxation of the dislocations, a microstructural analysis of the material under three different conditions was conducted. Figure 2 shows representative SEM-ETD images of the samples under the various conditions.

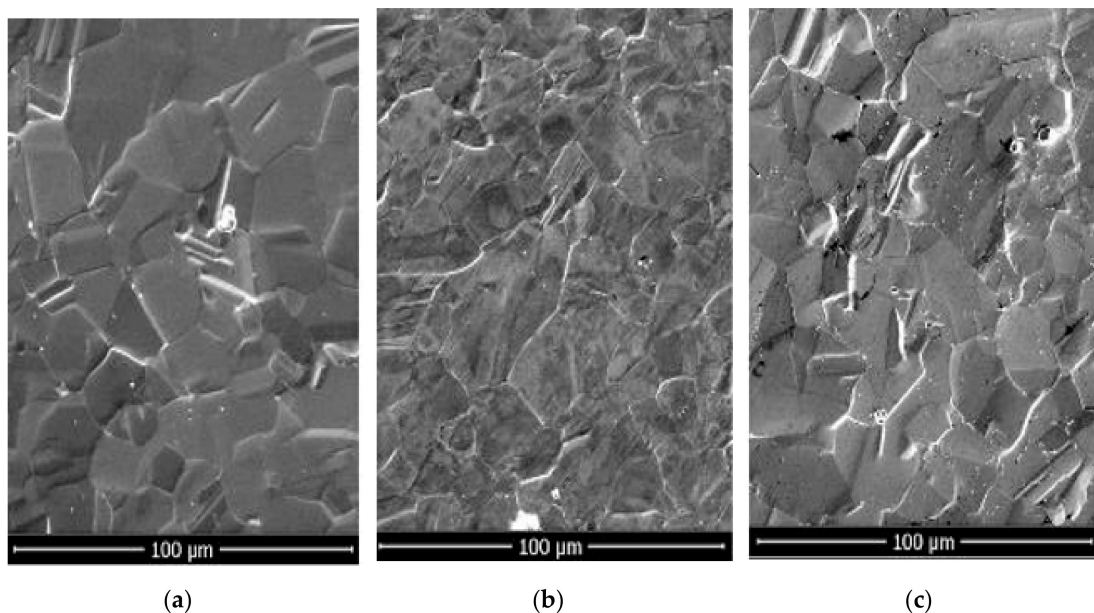


Figure 2. SEM-ETD images of the microstructure of the material under three different conditions. (a) AR condition, (b) after stretching the material to 50% of its stretching capacity and (c) after the intermediate annealing process (PSTT condition). The images were taken in the RD&ND direction (on the section plane between the rolling direction and the normal direction).

The averaged grain size of the samples remains on the 5 ASTM with a deviation of 1 ASTM. On the one hand, this is on the boundary of the supplier specifications, and on the other hand, this denotes that neither the TT and the pre-strain has deformed excessively the grain size.

Based on these observations, there were no obvious microstructural changes in the samples under the different conditions, suggesting that no critical microstructural changes were introduced during the annealing process. The results also indicated that only the dislocation density played a role in the elasto–plastic behaviour of the material. These results were expected as the holding time and temperature specifications used in this study were taken from an aeronautical handbook. Thus, these variables were not expected to modify the microstructure beyond stress relaxation.

Next, we investigated the changes in the behaviour in the elasto–plastic strain–stress state.

3. Characterization of Mechanical Properties of the Material

To characterize the elasto–plastic behaviour of the Inco718 material, we analysed its elastic behaviour and plasticity-induced evolution in this behaviour, followed by an analysis of plastic yielding and plastic flow. The hardening behaviour and Bauschinger effect were then experimentally observed. The necking limit of the material, characterized by its forming limit curve (FLC), was then evaluated. Furthermore, the surface texture and the impact of this texture on the friction coefficient were evaluated.

3.1. Elastic Behaviour

Dislocation pile-up can lead to non-linear hysteresis behaviour during unloading and loading cycles after plastic stretching of material [13]. Figure 3 shows a schematic of the behaviour of Inco718 in a loading–unloading test designed to characterize the material’s non-linear behaviour.

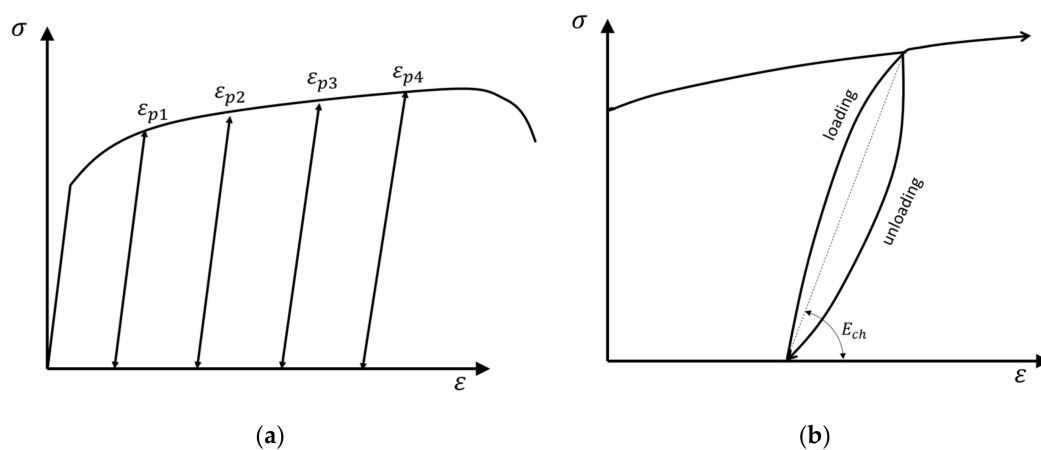


Figure 3. Schematic representation of the elastic modulus degradation testing in where: (a) loading–unloading test and (b) a hysteresis loop observed during the elastic unloading–loading step.

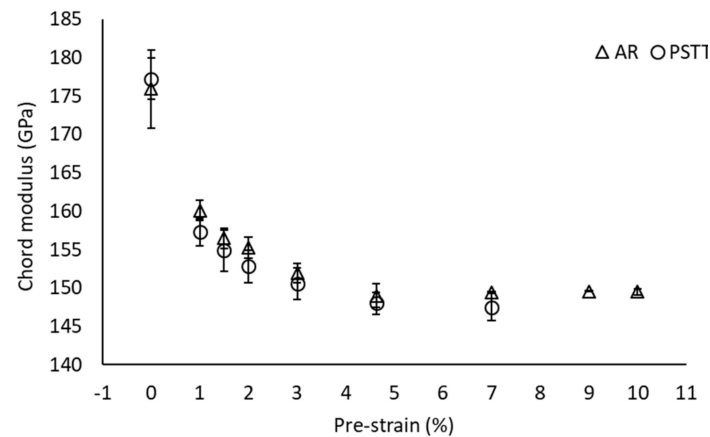
During this test, a standard tensile sample was stretched until a pre-defined pre-strain value (ϵ_{p1}). The sample was unloaded until zero stress was reached and then loaded again up to the pre-strain ϵ_{p1} value. Next, the sample was unloaded again, and the cycle was repeated, increasing the pre-strain level at each loop. A schematic representation of this process and the results obtained are shown in Figure 3a. As shown by an analysis of the elastic unloading–loading (Figure 3b), the unloading (and loading) path followed non-linear behaviour, creating a hysteresis loop. The modulus of the slope linking the start and finishing points of the loop was then measured (i.e., the chord modulus, E_{ch}).

Usually, the value of the chord modulus decreases with an increase in the pre-strain of the loop. In the present study case, the value of the chord modulus in both sets of samples (AR and PSTT) decreased from about 176 GPa at the first loading until around 150 GPa after 7% to 10% of plastic strain. At least three samples were tested under each condition, and the average value is shown in Table 3. The strain measurement of the samples was conducted using high-elongation strain gauges glued to the centre of the tensile specimen.

Table 3. Chord modulus evolution of the Inco718 material.

Pre-Strain	0%	1%	1.5%	2%	3%	4.5%	7%	9%	10%
AR (GPa)	176	160	156	155	152	149	149	149	149
PSTT (GPa)	177	157	155	153	151	148	148	-	-

Figure 4 shows the evolution of the chord modulus (with the deviation of the values as error bars) for both states (AR and PSTT).

**Figure 4.** Chord modulus evolution in the AR material and PSTT material.

As shown in Figure 4, similar changes were observed in the chord modulus behaviour of the AR and PSTT samples. The latter may suggest that the annealing process completely dissolved dislocation and that dislocation pile-ups were responsible for the hysteresis loops in the initial material state, at least in terms of the material's elastic behaviour. However, the chord modulus, which is commonly used to denote the equivalent elastic modulus, rapidly decreased in the first 4% to 5% of pre-strain and reached an asymptotic value of around 150 GPa. It is worth noting that the initial equivalent elastic modulus (chord modulus of the first loading) was 20 GPa lower than that specified by the material supplier. This is consistent with previous observations on high-strength steel when measuring using strain gauges and taking into account the non-linearity of the first loading [14,15]. This difference could have an impact on springback simulations [16].

3.2. Plastic Yielding and Plastic Flow

To experimentally evaluate the plastic yielding and plastic flow of the material, we conducted a tensile test. The test parameters were as follows: rolling direction (RD), 45 degrees to the RD (45D) and transversal direction (TD) to the RD. To evaluate the width strain and longitudinal strain simultaneously, a digital image correlation GOM-Aramis 5M system was used. The through-thickness strain was calculated based on the width strain and longitudinal strain values and assuming a constant volume, and the anisotropy coefficient or r -value was calculated. Using linear regression, the values were calculated between 10% and 20% of plastic strain. Table 4 shows the mean values of the three samples. These values were considered representative of the plastic flow of the material.

Table 4. Anisotropy coefficients of the Inco718 material (mean value, where the deviation was less than 0.03 in all cases).

State	RD	45D	TD
AR (-)	0.616	1.043	1.085
PSTT (-)	0.766	0.983	0.981

As shown in Table 4, there was no significant difference between the AR and PSTT behaviour of the samples. The largest difference between both states was found at RD (0.15 of difference). However, the difference was not remarkable from a practical point of view.

To evaluate the role of plastic yielding in triggering a stress state, the $R_{p0.2}$ was calculated in each direction (RD, 45D and TD). In addition, to analyse the potential non-symmetry of the plastic contour, plastic yielding triggering stresses were calculated under compression loads using an anti-buckling device [17]. Table 5 shows the tension and compression values in each direction.

Table 5. Yield stress values of the Inco718 material under different directions and load conditions.

State	RD		45D	TD	
	Tensile	Compression	Tensile	Tensile	Compression
AR (MPa)	431 ± 2.1	441 ± 1.9	448 ± 0.8	449 ± 2.0	457 ± 1.9
PSTT (MPa)	422 ± 2.3	435 ± 4.0	434 ± 2.7	434 ± 2.2	456 ± 2.5

Differences under 3% were found between the values of AR and PSTT. In terms of non-symmetry of the plastic contour, the difference was less than 5%.

Similar to the plastic flow and elastic behaviour, no appreciable difference was observed between the AR and PSTT states. Therefore, the use of a symmetric surface will not introduce too much error, as reviewed by Lewandowski et al. [18].

3.3. Hardening Behaviour

Two main characteristics of the hardening behaviour of a material are typically evaluated: stress–strain behaviour under monotonic stretching and the existence of a Bauschinger effect under strain path changes.

Figure 5 shows both characteristics for Inco718. Figure 5a illustrates the characteristic stress–strain relation in samples ($n = 3$) of the stretched material in both states (AR and PSTT), and Figure 5b shows the stress–strain relation under a strain path change at 2% of pre-strain.

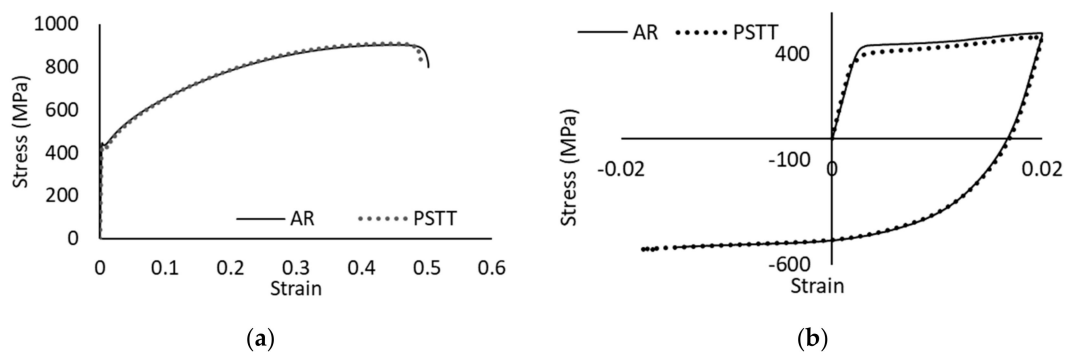


Figure 5. Hardening behaviour of the Inco718 material. (a) Monotonic stress–strain relation (engineering stress–strain) and (b) strain path change and stress–strain relation.

As shown in Figure 5a,b, both material states (AR and PSTT) exhibited the same hardening behaviour. The similar hardening behaviour is in accordance with the values found in the previous experimental tests. The Bauschinger effect was observed in both states (Figure 5b), with early yielding observed almost when the stress state started in compression. This phenomenon could be critical for accurate predictions of stresses under strain path changes.

3.4. Formability

The necking limit, often denoted by the FLC (forming limit curve), is a critical characteristic of all sheet material subjected to deep drawing operations. The FLC represents the limiting stretching

value where necking occurs under different strain paths (major and minor strain ratios). The FLC is determined in a Nakajima test, according to the ISO 12004 standard. The aim of intermediate annealing processes is to restore the initial material state and, therefore, improve the stretchability of the material allowing a restoration of the formability diagram.

Formability was analysed in Nakajima experiments, following the ISO 12004 standard for testing and post-processing methodology. Figure 6a shows the geometries of the samples, with each of these leading to a different strain path.

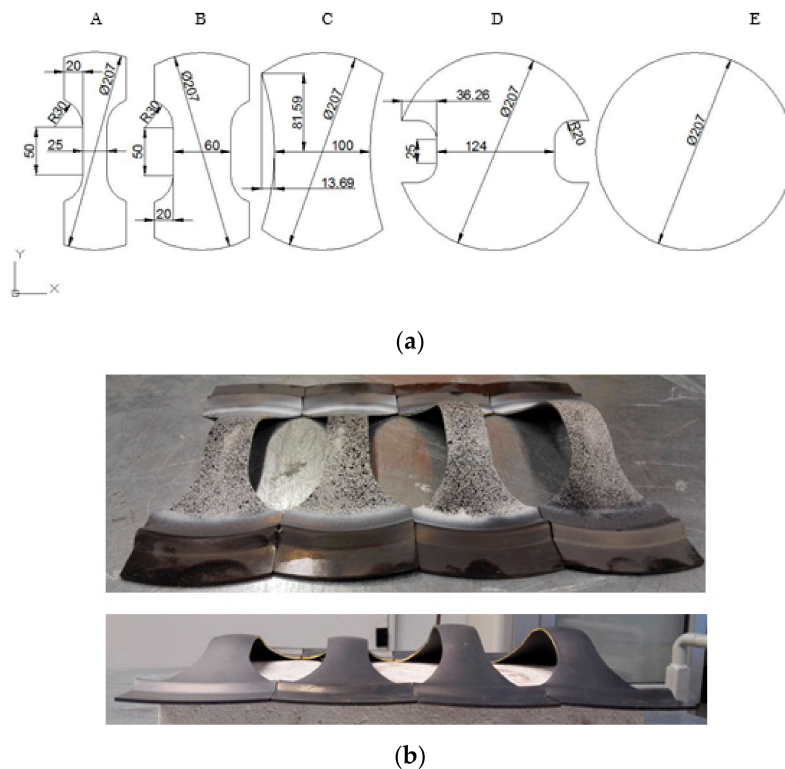


Figure 6. Forming limit of Inco718 samples. (a) Sample geometry and (b) pre-strain samples.

The testing procedure and sample preparation for the PSTT samples in the present study differed somewhat to those used in previous studies. The procedure was as follows: First, the standard FLC characterization of the AR samples was conducted. Following this procedure, a necking limiting point was obtained for each sample geometry (A, B, C, D and E). To conduct the pre-strain of the PSTT samples, the samples with different geometries were then drawn until 25% of the strain path of that geometry was reached. Next, the intermediate annealing process was carried out, and the samples were subsequently drawn until necking only, taking into account the strain values introduced in the second drawing step. For example, if a sample that followed a ‘plane strain’ path had a limiting strain at 0.3 of major strain (in the AR condition), for pre-stretching, the sample was drawn until 0.075 of major strain was obtained. The sample was then annealed and subsequently drawn until its necking limit was reached. If the sample reached 0.3 of the major strain after annealing, 0.075 was its pre-strain major strain, and an extra 0.3 of major strain was withstood before necking occurred. Thus, the total deformation was 0.375 using the annealing procedure. Figure 6b shows the samples after pre-strain.

To evaluate the capability of stretching of the Inco718 material under both AR and PSTT conditions, the FLC value of the AR material and that of the PSTT, taking into account only the strain introduced after intermediate annealing, were calculated. The results are shown in Figure 7.

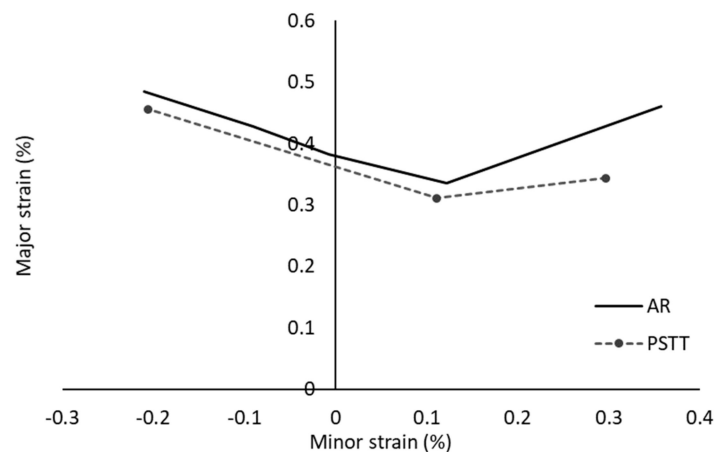


Figure 7. FLC of the Inco718 material. The continuous lines show the FLC of the AR necking limit, and the dashed lines denote the PSTT necking limit.

In accordance with standard industrial procedures for the cold stamping of materials, a graphite-based lubricant was used and a centred crack on the middle of the dome. GOM ARAMIS software was used for the online strain measurement and ISO standard application.

As shown in Figure 7, the minimum value point, theoretically the ‘plane strain’ point, was on the right side of the graph, even with a material thickness of 1.645 mm and a punch of 100 mm in diameter. These values may be explained by the theory of Min et al. [19]. As the objective of the present study was to compare the behaviour of both states (AR and PSTT), these values were accepted and included in the analysis.

As shown by the left part of the FLC, in contrast to the findings of previous experiments, there is a difference in the necking capacity on the biaxial strain path. Li et al. [20] observed a similar trend in a study on AA5182-O before and after intermediate annealing. They argued that the necking limiting strain under the biaxial strain state was close to the fracture point and that this made it difficult to determine whether the evaluated value was the necking point. With the results in hand, more comprehensive analyses are needed to shed light on this issue.

3.5. Friction Characterization

Apart from material behaviour, friction between the die and sheet also plays a key aspect in drawing operations. According to previous research, this friction was highly dependent on the lubricant, sheet, die surface roughness and material, as well as on contact pressure, sliding velocity and temperature [7].

In this study, the die material used was F-522T. The dies were polished in a toolmaker partner to give a final surface quality of $0.22 \mu\text{m Ra}$ and $1.34 \mu\text{m Rz}$. In a strip drawing test, the dies were used in conjunction with strips of the Inco718 material under different pressures ranging from 1 MPa to 40 MPa at a constant speed of 10 mm/s at room temperature.

Prior to the strip drawing test, surface strips of each sample covering an area of $3250 \times 3040 \mu\text{m}^2$ was analysed using a Sensofar S Neos with a $20\times$ objective, sampling of $0.65 \mu\text{m}$ and vertical resolution of 8 nm. Figure 8 shows the topographical analysis of the surfaces of the samples. Figure 8a,c shows the values for the AR sample, and Figure 8b,d depicts the values for the PSTT sample.

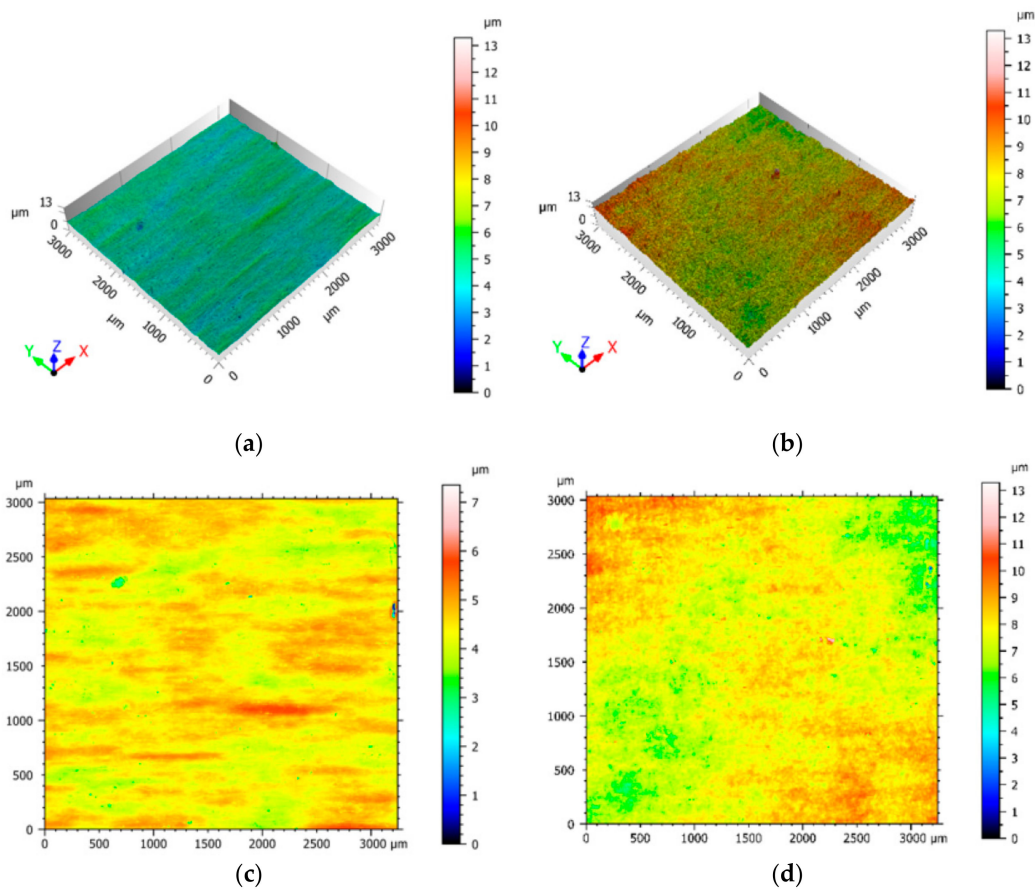


Figure 8. Topographic view of the material surface. (a,c) 3D and 2D representations of the surface of the AR material, respectively. (b,d) 3D and 2D representations of the surface of the PSTT material, respectively.

To evaluate differences between the surfaces, the S_q (the root mean square value of ordinate values) and S_{dr} (the developed interfacial area ratio) values of the surfaces were calculated. The results are shown in Table 6.

Table 6. Quantitative comparison of the surface of the AR material and that of the PSTT material after 7% pre-strain.

State	S_q (μm)	S_{dr} (μm)
AR	0.38 ± 0.04	0.48 ± 0.02
PSTT	0.79 ± 0.02	1.01 ± 0.06

Pre-strain of the sample and subsequent TT modified the surface roughness, increasing the S_q value from 0.38 to 0.79 and the S_{dr} value from 0.48 to 1.01. The increase in these values could affect the friction and wear behaviour of the material.

To evaluate the impact of changes in these values on friction behaviour, strip drawing tests were conducted. In the strip drawing tests, G-Start graphite spray and Condat Vicafil TFH4002 lubricant, which is commonly used in material drawing operations, were used. During the test, a strip of the sheet material under analysis is pressed between two square flat dies in order to apply the desired contact pressure. Once the pressure is achieved, the strip is pulled, and a relative displacement between the dies and the sheet is generated in which both forces—the pulling force and the normal force—are measured in order to calculate the existing friction coefficient on the tribological system. Further details

of the system can be found in [21]. The friction coefficient values obtained in the strip drawing tests are shown in Table 7.

Table 7. Strip drawing test friction coefficient values for both material surfaces at different contact pressures.

State	1 MPa	2.5 MPa	5 MPa	10 MPa	15 MPa	20 MPa	25 MPa	30 MPa	40 MPa
AR	0.037	0.022	0.009	0.007	-	0.011	-	0.014	0.016
PSTT	0.034	0.020	0.013	0.010	0.011	-	0.013	-	-

As shown in Table 7, even with an increase in surface roughness, the differences in the friction coefficient values of both material states (AR and PSTT) were negligible. Furthermore, the friction coefficient value obtained for the combination of materials and lubricant was low (<0.08). Changes in the coefficient of friction are shown in Figure 9.

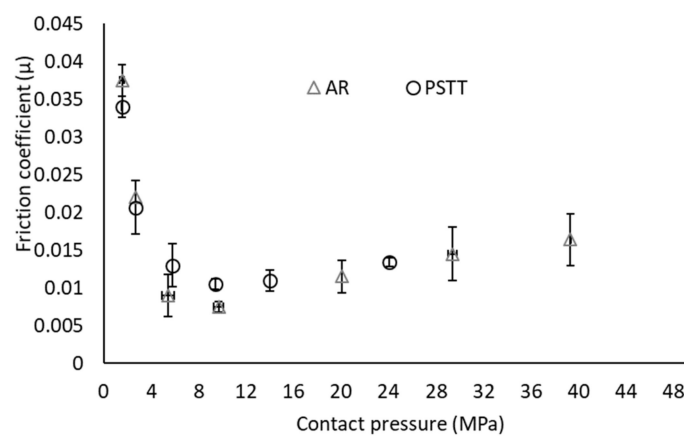


Figure 9. Evolution of the coefficient of friction measured during the strip drawing test under different contact pressures.

As shown in Figure 9, the friction coefficient rapidly decreased in the first 8 MPa, followed by saturation at a value of around 0.01. In the figure, the slight increase starting at 20 MPa may have been due to lubricant slippage. The high viscosity of the used lubricant usually creates a lubricant film, preventing contact between both surfaces. Therefore, in the first range of pressures (from 0 MPa to 20 MPa) the interaction behaviour is related to the behaviour of the lubricant under different pressures. However, under high pressures, the lubricant slips between the surfaces, remaining only in the valleys of the topography, and the tribological system changes as the contact of asperities can develop. However, further studies are necessary in order to clarify the origin of the increase in friction behaviour.

Based on the results obtained, with the exception of the necking limit for the biaxial strain path, in all other aspects, the intermediate annealing process restored the initial material state. Therefore, the behaviour of the PSTT material was similar to that of the AR material.

4. Material Modelling

After characterizing the properties of the material, deep drawing finite element software AutoForm[®], a commonly used commercial software, was used. The work focuses on models available in the software (with which we will later simulate the benchmark test). Similar to the material characterization, the modelling covered the elastic behaviour, plastic yielding and flow and hardening of the material.

4.1. Elastic Behaviour Modelling

There are three levels of simulation complexity when modelling the elastic behaviour of metals in deep drawing. The simplest type of simulation complexity involves the use of a constant modulus (Young's modulus) with linear elastic behaviour. The second level of simulation complexity involves the use of linear elastic behaviour but with an evolving elastic modulus. Usually, the chord modulus is taken as a reference [22]. The third level of simulation complexity involves the use of non-linear elastic behaviour with evolution due to plasticity [15]. In terms of the last level, there are three main models: the models of Yoshida [23], Wagoner [24] and Mendiguren [14]. However, none of these models are currently cost-efficient for use in industrial deep drawing simulations. The main model used in this second level of complexity is the model known as Yoshida's model. This model can be found in many scientific contributions in the last decade (e.g., [22]). The model predicts an asymptotic decrease in the elastic modulus defined as below:

$$E_{\text{ch}} = E_0 - (E_0 - E_a)(1 - \exp(-\gamma \bar{\epsilon}^P)), \quad (1)$$

where E_{ch} represents the chord modulus, E_0 is the initial modulus, E_a is the saturated modulus, $\bar{\epsilon}^P$ is the accumulated plastic strain, and γ is the saturation rate parameter of the model.

In the present study, the model coefficients that best suited the behaviour described in Figure 4 were as follows: E_0 of 177 GPa, E_a of 150 GPa and γ of 100.

4.2. Yield Criteria

Different hypotheses can be assumed regarding the flow rule, associated flow rule or non-associated flow rule [25]. Although some researchers favour the non-associated assumption, the association of the plastic potential to the yield criteria is commonly assumed. The yield criteria not only have to satisfy the limit stress states where plasticity is triggered but also have to govern the plastic flow of the material due to the normality rule.

Numerous yield functions, such as Hill49, Yld89, Yld2000-2D and BBC2008, have been formulated in the last decade [26]. In the present study, as proposed by previous authors [2], the Hill48 function was used to model the yielding behaviour of Inco718, as below:

$$2(\sigma_e)^2 = (G + H)\sigma_{11}^2 + (F + H)\sigma_{22}^2 - 2H\sigma_{11}\sigma_{22} + 2N\sigma_{12}^2, \quad (2)$$

where G , H , F and N are the model coefficients. At stress level, σ_{ij} correspond to the stress tensor ij component and σ_e represents the equivalent stress. When defining the coefficient to fit the r -values of the material, they were calculated as below:

$$G + H = 1, \quad (3)$$

$$F = (r_0)/(r_{90}(1 + r_0)), \quad (4)$$

$$G = 1/(r_0 + 1), \quad (5)$$

$$N = ((1 + 2r_{45})(r_0 + r_{45}))/ (2r_{90}(1 + r_0)). \quad (6)$$

In the above equations, r_0 , r_{90} and r_{45} represent the anisotropy coefficient at RD, TD and 45D, respectively.

Once the model was fitted to represent the r -values, it was checked to determine whether it accurately represented normalized yield stress ratios. In Figure 10, the accuracy of the Hill48 prediction is shown.

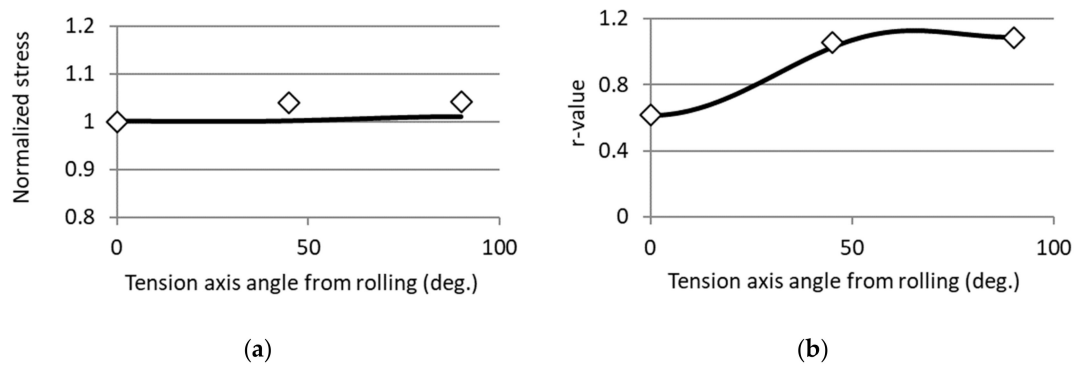


Figure 10. Anisotropic behaviour of the material in where: (a) normalized yield stresses using the Hill48 yielding function and (b) r -values. The markers show the experimental values, and the continuous line shows the model prediction.

Although the model was fitted using only the r -values, it predicted the yield stress relatively well. The low level of anisotropy at the yield stress values suggested that the model was representative of the behaviour of Inco718.

4.3. Hardening Law

There are various hardening laws described in the literature (e.g., Voce, Swift, Ludwik, Hollomon, Ghosh and Hockett-Sherby) [27]. Ragai [11] proposed the use of the hardening models of Ludwik and Hollomon. In the present study, after analysing the fitting accuracy of each model to the specific behaviour of Inco718 [11], we selected the model of Swift. According to this model, the hardening stress, σ_y , was defined as follows:

$$\sigma_y = K(\varepsilon_0 + \bar{\varepsilon}^P)^n, \quad (7)$$

where K , ε_0 and n are the model parameters, with values of 1.951 MPa, -0.09 and 0.299 , respectively. The idea is to use the experimental data up to the necking limit and to use Swift's model to extend that data up to the necessary strain. In this way, the negative value of ε_0 did not pose a problem, as the model only started from around 40% of plastic deformation.

Previous studies used different models to analyse the Bauschinger effect. As the present study used AutoForm software, we used the kinematic hardening model included with the software. Using the fitting tool of the software, the model parameters were 0.005 for the κ parameter and 0.29 for the ξ parameter.

5. Benchmark Analysis

To validate the developed models; a benchmark test was carried out under different holding forces and material states (AR and PSTT). The accuracy of the predicted final shapes (i.e., after springback) with different material models was then evaluated.

5.1. U-Drawing Test Set-Up

The U-drawing test is a commonly used benchmark test for springback simulations. In this test, a 90-degree square U channel is first drawn. When the material is released from the die, characteristic springback occurs [28]. The results of the test are primarily controlled by the die geometry, stroke and blank holding force (BHF). Figure 11 shows a schematic representation of the U-drawing test set-up used in this study.

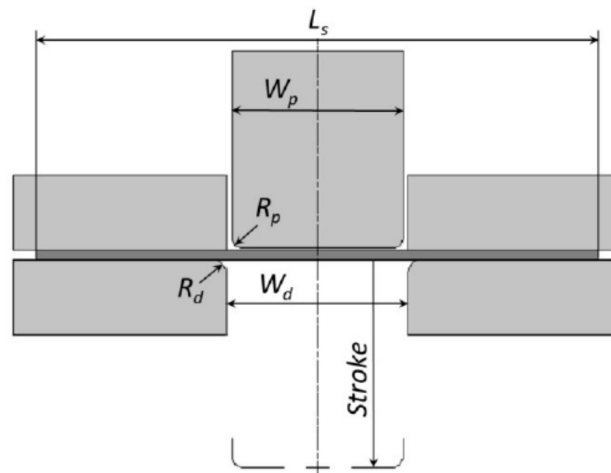


Figure 11. U-drawing test schematic.

During the test, a strip 330 mm long and 110 mm wide was clamped between the blank holder and the die (radius of 8 mm and opening of 106 mm) and then drawn with the punch (radius of 5 mm and width of 100 mm). Details of the test set-up are shown in Table 8.

Table 8. Parameters of the U-drawing experimental test.

W_p (mm)	R_p (mm)	R_d (mm)	W_d (mm)	L_s (mm)	Stroke (mm)
100	5	8	106	330	35-70

Two different BHF's were used to try to generate different strain states during the drawing step: a low BHF (L-BHF) of 8 t and a high BHF (H-BHF) of 28 t.

In the benchmark test, the pre-strain conditions were in accordance with industrial standards. In the AR test condition, the sheet was directly drawn to 70 mm of stroke. In contrast, in the PSTT condition, the sheet was first drawn to 35 mm of stroke. The resulting channel from that step was then annealed following intermediate annealing conditions. Finally, the annealed component was drawn up to 70 mm.

The resulting channels were measured using a coordinate-measuring machine to obtain the final post-springback profile. In this step, the channels were clamped in a central line (a symmetry line), and the profile was then measured.

Figure 12 shows the resultant profiles of the AR and PSTT materials under the different BHF's (L-BHF and H-BHF). Only a representative profile of three tested samples is shown.

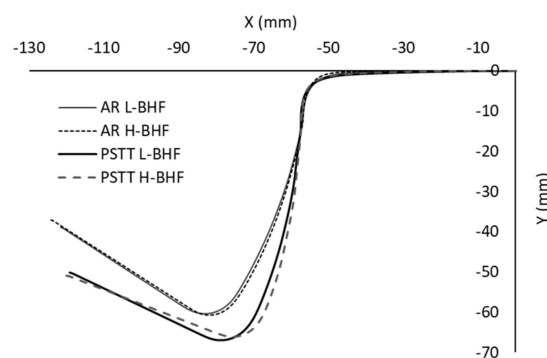


Figure 12. Experimental representation of the resultant channels after springback in the AR and PSTT materials under low blank holding forces (L-BHF's) and high blank holding forces (H-BHF's).

As shown in Figure 12, the holding force did not have a strong impact on springback. Although there was a slight difference in springback of the PSTT material at L-BHFs and H-BHFs, the difference could be due to the positioning on the coordinate-measuring machine scatter. The intermediate TT had a marked impact on the final springback of the U channel.

5.2. Analysed Material Models

Various models of the material and its components (i.e., elasticity, yielding and hardening) were developed and analysed. Table 9 provides a summary of the analysed models. The most basic model (Iso model) included a constant elastic modulus with Hill48 yielding and isotropic hardening. Another model, the kinematic model, included the Bauschinger effect of the material and hardening. A third model was composed of the basic model (Iso) but included a decrease in the elastic modulus (Young). The last and more complex model, referred to as 'full', took into account both the decrease of the elastic modulus and the Bauschinger effect.

Table 9. Summary of the analysed models.

Model Designation	Elasticity	Yielding	Hardening
Iso	Constant	Hill48	Isotropic
Kinematic	Constant	Hill48	Isotropic + kinematic
Young	Variable	Hill48	Isotropic
Full	Variable	Hill48	Isotropic + kinematic

5.3. Friction Model

As shown in Figure 9, the friction coefficient changed with the contact pressure. This type of evolving friction coefficient can be modelled in a variety of ways. On the one hand, one could assume a constant coefficient was valid for a certain range. On the other hand, specific variable friction coefficient laws, such as that of Filsek, could be used [7].

The contact pressure generated by the L-BHF and H-BHF (σ_p) was calculated, taking into account that the surface of the sheet in contact with the die/blank holder declined during the drawing. According to the calculation, the L-BHF pressure varied between 4 MPa and 8.25 MPa, and the H-BHF pressure varied between 12 MPa and 27 MPa. When the friction coefficient values (μ) were analysed at the pressure ranges used in the present study (Figure 9), the coefficient was approximately constant.

$$\text{BHF} = 8 \text{ t} \rightarrow \sigma_p = 4.0 - 8.25 \text{ MPa} \rightarrow \mu = 0.009, \quad (8)$$

$$\text{BHF} = 28 \text{ t} \rightarrow \sigma_p = 12.0 - 27.0 \text{ MPa} \rightarrow \mu = 0.0115. \quad (9)$$

Thus, a constant coefficient of friction was used in the simulation. One coefficient was used in the L-BHF models, and a different one was used in the H-BHF models.

5.4. FEM Model

As previously stated, Autoform[®] commercial software was used for the numerical simulations. The tools were assumed to be rigid in contrast to the sheet that was discretized in first-order four-node shell elements. These elements were numerically integrated through thickness using 11 integrations points with six levels of refinement. The average size of the elements was defined to be 20 mm. The standard Autoform[®] 'final validation' convergence tolerances were used, aiming at reproducing the industrial standard.

6. Results and Discussion

In the present study, we compared the springback shape predicted by the models and that experimentally obtained. Figure 13 shows the comparison for the AR H-BHF as a reference. To illustrate

the differences between the models in terms of springback predictions, the whole channel is shown in Figure 13a, where only the flange area of the left side of the channel is depicted in Figure 13b. In these figures, X and Y represent space coordinates.

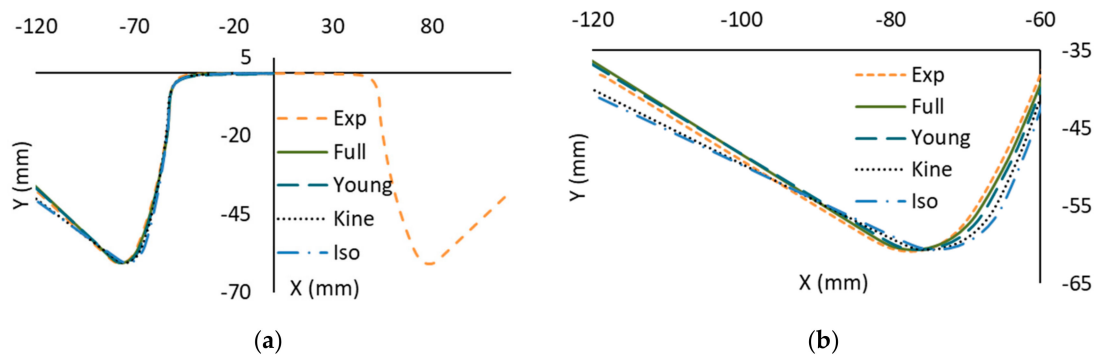


Figure 13. Springback prediction of the different models for the AR H-BHF case. (a) Whole profile and (b) left side of the profile.

As can be seen from the results, the full and Young models had the highest accuracy. To evaluate the accuracy of each model in every case, the springback angle $\Delta\theta_i$ (final angle minus 90 degrees of the forming angle) was evaluated for each model and analysed case. The angle measurement followed the protocol defined in the Numisheet benchmark of 1993 [28]. Table 10 summarises the values of the springback angles.

Table 10. Summary of the springback angles after forming for each model and experiment.

Material State	Model	L-BHF		H-BHF	
		$\Delta\theta_1$	$\Delta\theta_2$	$\Delta\theta_1$	$\Delta\theta_2$
AR	Exp	7.6	3.45	7.28	3.45
	Full	7.31	2.14	7.02	2.56
	Young	6.92	1.82	6.39	1.12
	Kine	5.44	1.85	4.66	0.57
	Iso	4.84	0.29	4.36	0.34
PSTT	Exp	2.04	4.13	1.56	3.85
	Full	1.18	3.65	0.77	3.02
	Young	1.06	1.15	0.53	1.24
	Kine	0.25	0.98	0.43	0.75
	Iso	0.18	-0.04	0.21	0.67

In the case of the PSTT, the simulations were carried out as follows:

- (a) The first drawing was simulated using the AR material model (35 mm drawing).
- (b) The springback of that step was then simulated.
- (c) Next, the post-springback geometry was imported, without any residual stress or strain, and the second drawing (until reaching a drawing depth of 70 mm) was performed with the AR material model.
- (d) Finally, the last springback was simulated.

To evaluate the accuracy of each model, the error of accuracy (in %) between the predicted springback angle and experimental springback angle was calculated. Figures 14 and 15 show the accuracy of the springback angle prediction for $\Delta\theta_1$ and $\Delta\theta_2$, respectively.

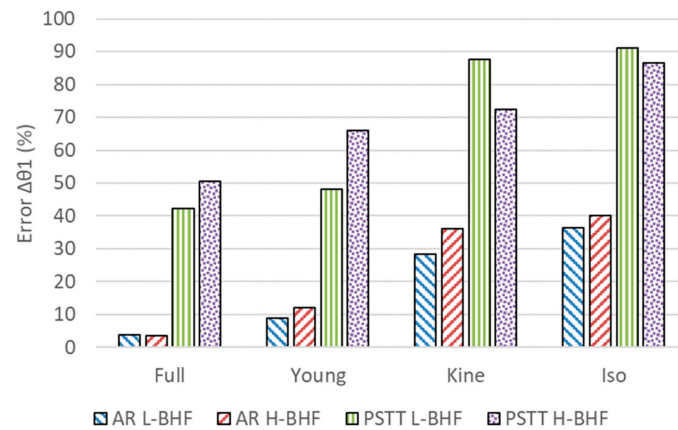


Figure 14. Accuracy of the different models in terms of the $\Delta\theta_1$ springback angle.

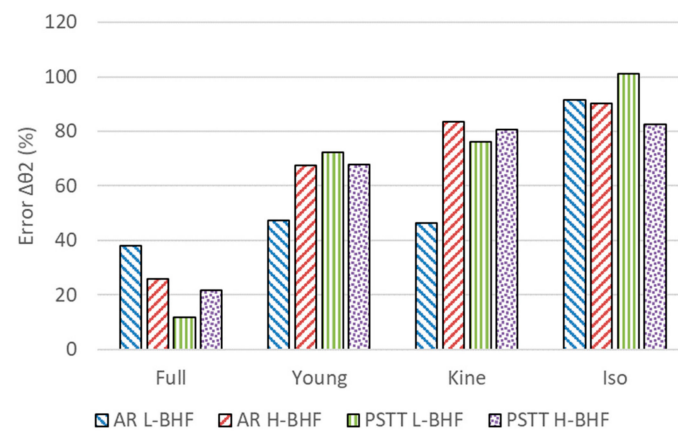


Figure 15. Accuracy of the different models in terms of the $\Delta\theta_2$ springback angle.

From the results, it can be concluded that, in every case, the full model was the most accurate, followed by the Young model. This was expected as the full model was the most complete one. However, for the PSTT, at a H-BHF, errors of up to 50% were found in the $\Delta\theta_1$. In terms of the springback angle, the angles differed in the various models between 91.57 degrees and 90.77 degrees. However, these values were within the accuracy of springback simulations of sheet metal forming [16].

7. Conclusions

In this study, Inco718 material was characterized in a deep drawing process with and without intermediate annealing TTs. In addition, material models were developed, and their accuracy was evaluated using a U-drawing benchmark test. Based on the findings, the following conclusions can be drawn:

- The intermediate annealing process restored the initial properties of the material, with the exception of the biaxial necking limit.
- Failure to restore the biaxial necking behaviour could be due to fracture measurements; further investigations are necessary to clarify this issue.
- The apparent elastic modulus of the material markedly decreased reaching the 150 GPa after 4% to 5% of plastic pre-strain.
- Although the flow behaviour of the material was anisotropic, isotropic-like behaviour was observed under conditions of yield stress.
- The tension compression test revealed an important impact of the Bauschinger effect.
- Taking into account all the features of the material. The evolution of the elastic modulus and the Bauschinger effect was found to be the key phenomena to model.

- Low-friction behaviour was obtained using the tool material, sheet material and lubricant combination.
- Although the roughness of the material increased during the pre-strain process, subsequent TT did not appear to affect the friction coefficient.

The main contribution of this work is to provide the community with a valid model to simulate the deep drawing process of the Inco718 material, with and without intermediate annealing steps.

Author Contributions: Experimental characterization of the material under different TT, U.U.; Numerical simulation of the process using AutoForm software, L.G.; Benchmark experimental testing, E.S.d.A.; Material model development and project supervision, J.M. All authors have read and agreed to the published version of the manuscript.

Funding: This research received no external funding.

Conflicts of Interest: The authors declare no conflicts of interest.

References

1. Bridges, D.; Xu, R.; Hu, A. Microstructure and mechanical properties of Ni nanoparticle-bonded Inconel 718. *Mater. Des.* **2019**, *174*, 107784. [[CrossRef](#)]
2. Groche, P.; Bäcker, F. Springback in stringer sheet stretch forming. *CIRP Ann.-Manuf. Technol.* **2013**, *62*, 275–278. [[CrossRef](#)]
3. Zhan, M.; Wang, Y.; Yang, H.; Long, H. An analytic model for tube bending springback considering different parameter variations of Ti-alloy tubes. *J. Mater. Process. Technol.* **2016**, *236*, 123–137. [[CrossRef](#)]
4. Cansino, J.M.; Román, R. Energy efficiency improvements in air traffic: The case of Airbus A320 in Spain. *Energy Policy* **2017**, *101*, 109–122. [[CrossRef](#)]
5. Mertin, C.; Stellmacher, T.; Schmitz, R.; Hirt, G. Enhanced springback prediction for bending of high-strength spring steel using material data from an inverse modelling approach. *Procedia Manuf.* **2019**, *29*, 153–160. [[CrossRef](#)]
6. Palm, C.; Vollmer, R.; Aspacher, J.; Gharbi, M. Increasing performance of hot stamping systems. *Procedia Eng.* **2017**, *207*, 765–770. [[CrossRef](#)]
7. Sigvant, M.; Pilthammar, J.; Hol, J.; Wiebenga, J.H.; Chezan, T.; Carleer, B.; van den Boogaard, T. Friction in sheet metal forming: Influence of surface roughness and strain rate on sheet metal forming simulation results. *Procedia Manuf.* **2019**, *29*, 512–519. [[CrossRef](#)]
8. Sirvin, Q.; Velay, V.; Bonnaire, R.; Penazzi, L. Mechanical behaviour modelling and finite element simulation of simple part of Ti-6Al-4V sheet under hot/warm stamping conditions. *J. Manuf. Process.* **2019**, *38*, 472–482. [[CrossRef](#)]
9. Algarni, M.; Bai, Y.; Choi, Y. A study of Inconel 718 dependency on stress triaxiality and Lode angle in plastic deformation and ductile fracture. *Eng. Fract. Mech.* **2015**, *147*, 140–157. [[CrossRef](#)]
10. Gustafsson, D.; Moverare, J.J.; Simonsson, K.; Sjöström, S. Modeling of the constitutive behavior of Inconel 718 at intermediate temperatures. *J. Eng. Gas Turbines Power* **2011**, *133*, 094501. [[CrossRef](#)]
11. Ragai, I. Experimental and Finite Element Investigation of Springback of Aerospace/Automotive Sheet Metal Products. ProQuest Dissertations and Theses. Ph.D. Thesis, McGill University, Montreal, QC, Canada, 2006.
12. Aerens, R.; Vorkov, V.; Dufloy, J.R. Springback prediction and elasticity modulus variation. *Procedia Manuf.* **2019**, *29*, 185–192. [[CrossRef](#)]
13. Kupke, A.; Madej, L.; Hodgson, P.D.; Weiss, M. Experimental in-situ verification of the unloading mechanics of dual phase steels. *Mater. Sci. Eng. A* **2019**, *760*, 134–140. [[CrossRef](#)]
14. Mendiguren, J.; Trujillo, J.J.; Cortés, F.; Galdos, L. An extended elastic law to represent non-linear elastic behaviour: Application in computational metal forming. *Int. J. Mech. Sci.* **2013**, *77*, 57–64. [[CrossRef](#)]
15. Mendiguren, J.; Cortés, F.; Gómez, X.; Galdos, L. Elastic behaviour characterisation of TRIP 700 steel by means of loading-unloading tests. *Mater. Sci. Eng. A* **2015**, *634*, 147–152. [[CrossRef](#)]
16. Wagoner, R.H.; Lim, H.; Lee, M.-G. Advanced Issues in springback. *Int. J. Plast.* **2013**, *45*, 3–20. [[CrossRef](#)]
17. Kuwabara, T.; Kumano, Y.; Ziegelheim, J.; Kurosaki, I. Tension-compression asymmetry of phosphor bronze for electronic parts and its effect on bending behavior. *Int. J. Plast.* **2009**. [[CrossRef](#)]

18. Lewandowski, J.J.; Wesseling, P.; Prabhu, N.S.; Larose, J.; Lerch, B.A. Strength differential measurements in IN 718: Effects of superimposed pressure. *Metall. Mater. Trans. A* **2003**, *34*, 1736–1739. [[CrossRef](#)]
19. Min, J.; Stoughton, T.B.; Carsley, J.E.; Lin, J. Compensation for process-dependent effects in the determination of localized necking limits. *Int. J. Mech. Sci.* **2016**, *117*, 115–134. [[CrossRef](#)]
20. Li, J.; Carsley, J.E.; Stoughton, T.B.; Hector, L.G.; Hu, S.J. Forming limit analysis for two-stage forming of 5182-O aluminum sheet with intermediate annealing. *Int. J. Plast.* **2013**, *45*, 21–43. [[CrossRef](#)]
21. Gil, I.; Mendiguren, J.; Galdos, L.; Mugarra, E.; Saenz de Argandoña, E. Influence of the pressure dependent coefficient of friction on deep drawing springback predictions. *Tribol. Int.* **2016**, *103*, 266–273. [[CrossRef](#)]
22. Eggertsen, P.-A.; Mattiasson, K. On the identification of kinematic hardening material parameters for accurate springback predictions. *Int. J. Mater. Form.* **2011**, *4*, 103–120. [[CrossRef](#)]
23. Sumikawa, S.; Ishiwatari, A.; Hiramoto, J.; Yoshida, F.; Clausmeyer, T.; Tekkaya, A.E. Stress state dependency of unloading behavior in high strength steels. *Procedia Eng.* **2017**, *207*, 179–184. [[CrossRef](#)]
24. Lee, J.; Lee, J.-Y.; Barlat, F.; Chung, K.; Wagoner, R.H.; Lee, M.-G. Extension of quasi-plastic-elastic approach to incorporate complex plastic flow behavior an application to springback of advanced high-strength steels. *Int. J. Plast.* **2013**, *45*, 140. [[CrossRef](#)]
25. Park, N.; Stoughton, T.B.; Yoon, J.W. A criterion for general description of anisotropic hardening considering strength differential effect with non-associated flow rule. *Int. J. Plast.* **2019**. [[CrossRef](#)]
26. Mendiguren, J.; Galdos, L.; de Argandoña, E.S. On the plastic flow rule formulation in anisotropic yielding aluminium alloys. *Int. J. Adv. Manuf. Technol.* **2018**, *99*, 255–274. [[CrossRef](#)]
27. Agirre, J.; Galdos, L.; Saenz de Argandoña, E.; Mendiguren, J. Hardening prediction of diverse materials using the digital image correlation technique. *Mech. Mater.* **2018**, *124*, 71–79. [[CrossRef](#)]
28. Galdos, L.; De Argandoña, E.S.; Mendiguren, J.; Gil, I.; Ulibarri, U.; Mugarra, E. Numerical simulation of U-drawing test of Fortiform 1050 steel using different material models. *Procedia Eng.* **2017**, *207*, 137–142. [[CrossRef](#)]



© 2020 by the authors. Licensee MDPI, Basel, Switzerland. This article is an open access article distributed under the terms and conditions of the Creative Commons Attribution (CC BY) license (<http://creativecommons.org/licenses/by/4.0/>).